

Hyperspectral Target Detection Method Based on Nonlocal Self-Similarity and Rank-1 Tensor

Chunhui Zhao, Mingxing Wang[✉], Shou Feng[✉], and Nan Su[✉]

Abstract—In recent years, many target detection methods based on tensor representation theory have been proposed and achieved good results for hyperspectral images (HSIs). However, these methods still have some deficiencies. For example, 3-D hyperspectral data are first transformed into 1-D vectors in these methods, which may destroy the spatial structure of HSI data and reduce the detection performance. Besides, when the number of training samples is small, the results of the target detection method usually become worse. To solve these problems, a hyperspectral target detection method based on nonlocal self-similarity and rank-1 tensor is proposed in this article. First, different from these traditional tensor representation-based methods, the third-order tensor data are directly used as the input of the proposed method to preserve the spatial information and structure of an HSI. Second, the tensor blocks related to the class are constructed by using the nonlocal self-similarity of HSI data. Finally, by taking advantage of rank-1 canonical decomposition attribute, the process of tensor operation can be simplified, and the number of training samples can be reduced. The proposed method is compared with six state-of-the-art hyperspectral target detection methods on four HSI data sets. The experimental results show that the proposed method can have better target detection results than other compared methods, especially in the case of fewer training samples.

Index Terms—Dictionary learning, hyperspectral target detection, nonlocal self-similarity, rank-1 tensor, tensor product.

I. INTRODUCTION

HYPERSPECTRAL imagery is obtained by measuring the reflection and radiation characteristics of the target on the earth's surface through a hyperspectral sensor. After processing, the obtained data can be used for classification, detection, and other purposes [1]. One pixel in a hyperspectral image can contain hundreds of measurements from the visible spectrum to infrared. Hyperspectral target detection technology can mark each pixel in the hyperspectral image as a target

Manuscript received August 21, 2020; revised October 27, 2020 and December 11, 2020; accepted January 7, 2021. This work was supported in part by the National Natural Science Foundation of China under Grant 61971153, Grant 62002083, Grant 62071136, and Grant 61801142; in part by the Heilongjiang Postdoctoral Foundation under Grant LBH-Z20038; and in part by the Heilongjiang Postdoctoral Funds for Scientific Research Initiation under Grant LBH-Q20085. (*Corresponding author: Shou Feng*)

The authors are with the College of Information and Communication Engineering, Harbin Engineering University, Harbin 150001, China, and also with the Key Laboratory of Advanced Marine Communication and Information Technology, Ministry of Industry and Information Technology, Harbin Engineering University, Harbin 150001, China (e-mail: zhaochunhui@hrbeu.edu.cn; wangmingxing11011@foxmail.com; fengshou@hrbeu.edu.cn; sunan08@hrbeu.edu.cn).

Color versions of one or more figures in this article are available at <https://doi.org/10.1109/TGRS.2021.3051204>.

Digital Object Identifier 10.1109/TGRS.2021.3051204

or background by distinguishing the materials of different objects, such as identifying military camouflage, underground fortifications, resource detection or environmental monitoring, and so on. Therefore, hyperspectral target detection technology has great significance in both military and civilian fields [2]–[6].

In order to effectively detect hyperspectral targets, researchers have done a lot of work, popular algorithms include the traditional methods based on spectral feature matching, methods based on sparse representation or machine learning, and methods based on tensor representation, which have attracted more attention. Traditional detection methods such as orthogonal subspace projection (OSP) were first applied in the field of target detection, but only using spectral information, the detection effect is not satisfactory. In recent years, by making use of the sparse properties of hyperspectral images, the methods based on sparse representation have been widely used in the field of hyperspectral image processing, and have become the mainstream of HSI target detection [7]–[9]. These algorithms make use of the sparse properties of hyperspectral images, and first establish a complete spectral dictionary, which usually contains hundreds of spectra, including target spectrum and background spectrum. Then, each pixel in the image is regarded as a linear combination of a small number of spectra in the spectral dictionary, and then the spectrum of the pixel to be measured is linearly represented by the joint dictionary (which is composed of the background end-member spectrum and the target prior spectrum) [10], [11]. Finally, the reconstruction error of sparse representation is compared to distinguish the pixel category.

It should be noted that in the method based on sparse representation, the constructed dictionary can only represent spectral information, and the key spatial-related information between each pixel cannot be expressed by spectral dictionary, and its target detection performance is greatly affected by the selection of training samples [12].

Researchers have proposed some hyperspectral image target detection methods based on machine learning algorithms, including support vector data description (SVDD) [13], regularization technology, fusion detector, support vector machine technology (SVM) [14], manifold learning [15], and deep learning [16]. The supervised metric learning algorithm (SML) [17] is one of the machine learning algorithms, which can effectively learn the distance metric of HSI target detection in a supervised way. Considering the spectral characteristics of the background sample and the target sample, the

distance metric generated by SML makes the target pixel easily detected in the target space, and the background pixel is placed in the background space as much as possible. The target detection algorithm based on transfer learning [18] uses transfer learning to save the discriminative information in the training data to test data that are not in the same feature space and the data distribution is different, and can learn the subspace from limited samples. Researchers have successively proposed some kernel-based detection algorithms [19]–[21].

The above method based on machine learning regards HSI data as first-order or second-order data, but this is not consistent with the reality, HSI data are actually third-order, including 2-D spatial information and 1-D spectral information. Making better use of the spatial and spectral information contained in HSI data can improve the performance of target detection [22], [23].

For HSI data, the new mathematical expression is used to mine the characteristics of the data. Using tensors to re-express hyperspectral images can simultaneously express the global information of the spatial spectrum of the hyperspectral images [24]. For example, Xiao *et al.* [25] used tensor representation to realize spatial target identification of hyperspectral images. The multivariate linear blind source spectral decomposition method based on tensor representation [26] decomposes the hyperspectral image into three-factor sets. They respectively represent spectral characteristics and 2-D spatial distribution, and can be easily applied to target recognition algorithms. In addition, researchers combine tensors with traditional target detection algorithms. For example, Su *et al.* [27] proposed a tensor matching subspace detector and applied it to target detection scenes.

In the method based on tensor representation, the input data are usually a vector, so it is necessary to perform tensor vectorization before target detection [28]. However, hyperspectral data contain 2-D spatial information and 1-D spectral information. Vectorization decomposes the 3-D tensor into 1-D vector through mathematical operation, which will destroy the spatial structure of the tensor, cause the loss of information, and cannot solve the high-dimensional problem of tensor data, and may add a large number of adjustable parameters may be added [29], [30].

In order to solve these problems, it is necessary to take the tensor data directly as the input, and then uses tensor operation to reduce the number of adjustable parameters. In this article, a hyperspectral target detection method based on nonlocal self-similarity and rank-1 tensor is proposed. The method parameter satisfies the rank-1 regular decomposition attribute, which means that the number of training samples needed by the method is significantly reduced, and the spatial structure information of HSI data can also be retained. The method is mainly divided into two parts. First, the HSI data itself are regarded as a third-order tensor, and they are divided into several full-band blocks. If these tensor blocks are grouped according to the target class or background class, the features of the same category are more similar. The second step is to sparsely represent each packet and obtain the constructed dictionary, and calculate the core tensor through tensor algebra operation. The category of test samples can be distinguished

by the minimum residual. To sum up, the contribution of this article has three aspects. The algorithm proposed in this article is referred as TBLD briefly.

- 1) In traditional methods based on tensor representation, the input data are usually a vector which may destroy the spatial structure of the tensor, cause the loss of information. Different from traditional methods of converting the original HSI data into vectors, the third-order tensor data are directly used as the input of the proposed method. Hyperspectral images contain second-order spatial information and first-order spectral information. At the same time, tensors can also contain third-order information. The third-order tensor can contain not only the second-order spatial information, but also the first-order spectral information, which can preserve the 3-D structure and the spatial information of the HSI data.
- 2) Traditional methods only use the label information in the residual discrimination process. Different from traditional methods, the TBLD method uses nonlocal self-similarity to obtain appropriate dictionaries. Nonlocal self-similarity makes full use of label information to obtain the sparse representation coefficient, which is more helpful to improve the detection performance.
- 3) The experimental results show that compared with the traditional method, the TBLD method has a better detection effect when there are only a few training samples. In the process of tensor algebra operation, the TBLD method uses rank-1 canonical decomposition attribute to better explain the influence of tensor data as input on target detection. The process of tensor operation can be simplified, and the number of training samples can be reduced, which is more suitable for the case that there are only a few training samples.

The arrangement of this article is as follows. In Section II, the theories of tensor operation, sparse representation, and tensor representation are described. In Section III, the proposed hyperspectral target detection method based on nonlocal self-similarity and rank-1 tensor is introduced in detail. The experimental results on four real data sets are reported in Section IV. Finally, a conclusion is drawn in the last section.

II. BRIEF INTRODUCTION TO PREVIOUS METHODS

In this section, the definitions of related symbols and some basic theories and methods are introduced, including sparse representation, tensor operation, and tensor representation.

A. Sparse Representation

First of all, it is necessary to clarify some mathematical definitions and symbols. In this article, the n -order tensor is represented by a bold curlicue letter, such as $\mathbf{Y} \in R^{i_1 \times i_2 \times \dots \times i_n}$, the vector is represented by a bold lowercase letter, such as $\mathbf{a} \in R^{i_1}$, the matrix is represented by a bold uppercase letter, such as $\mathbf{A} \in R^{i_1 \times i_2}$, and the scalar is represented by a lowercase letter, such as a .

Sparse representation is one of the common tools in hyperspectral image processing in recent years. It is assumed that

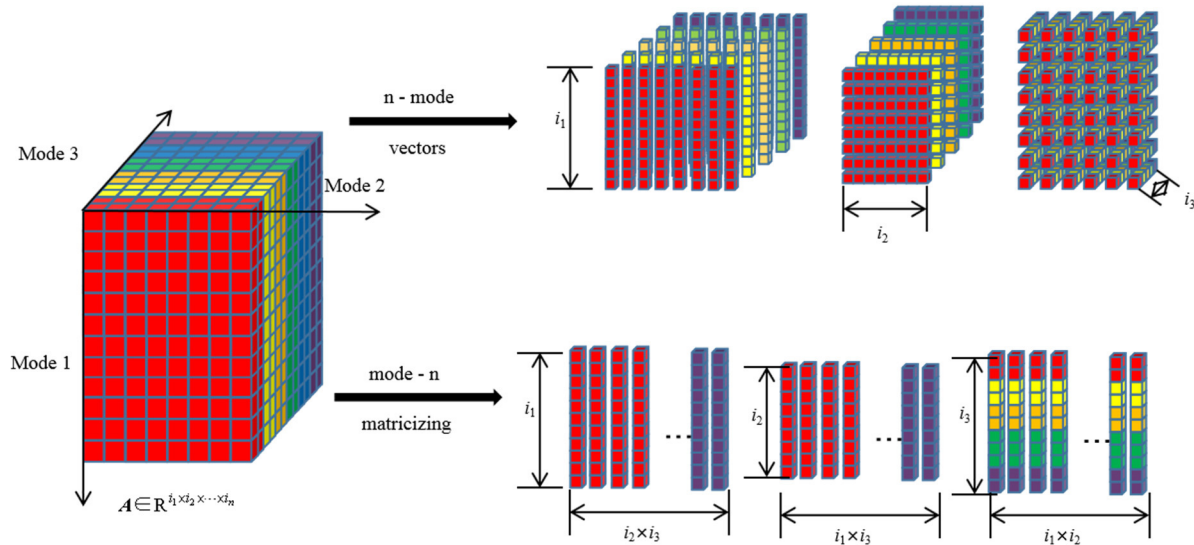


Fig. 1. Tensor decomposition and tensor matrixization of mode-n.

the unknown sample $x \in R^{l_s}$ can be represented by the training sample as

$$x = Dz \quad (1)$$

where $D = [D_1, D_2, \dots, D_k] \in R^{l_s \times k}$ is the dictionary obtained from class k training samples, l_s is the number of spectra, and z is the sparse coefficient [31]

$$\hat{z} = \text{argmin} \|z\|_0 \text{ s.t. } x = Dz. \quad (2)$$

Formula (2) can be solved by greedy algorithms, such as orthogonal matching pursuit (OMP).

After z is obtained, the category of the test sample can be determined by the residual [32]

$$\text{class } x = \arg \min_{k=1,2,\dots,c} \|x - D\hat{z}_k\|_2. \quad (3)$$

B. Notes and Definitions of Tensor Algebra

Tensor vectorization: Operator $\text{vec}(\cdot)$ represents tensor vectorization. If the tensor $A \in R^{i_1 \times i_2 \times \dots \times i_n}$ is mapped to a column vector, then the j entry $A = [\dots a_{i_1, \dots, i_n} \dots]$ of the $\text{vec}(A)$ map, where j can be expressed as

$$j = 1 + \sum_{n=1}^N (i_n - 1) \prod_{n'=1}^{n-1} i_{n'}. \quad (4)$$

Kronecker Product: If the tensors $A \in R^{i_1 \times i_2}$ and $B \in R^{i_3 \times i_4}$, then their Kronecker Product can be expressed as

$$A \otimes B = \begin{bmatrix} a_{11}B & a_{12}B & \dots & a_{1k}B \\ a_{21}B & a_{22}B & \dots & a_{2k}B \\ \vdots & \vdots & & \vdots \\ a_{j1}B & a_{j2}B & \dots & a_{jk}B \end{bmatrix} \in R^{(i_1 i_3) \times (i_2 i_4)}. \quad (5)$$

Rank-R decomposition: If tensor $A \in R^{i_1 \times i_2 \times \dots \times i_n}$ and $A = \sum_{r=1}^R a_1^r \circ \dots \circ a_n^r$, symbol \circ denote vector outer product, $a_c^r (c = 1, 2, \dots, n, r = 1, 2, \dots, R)$ is the element in

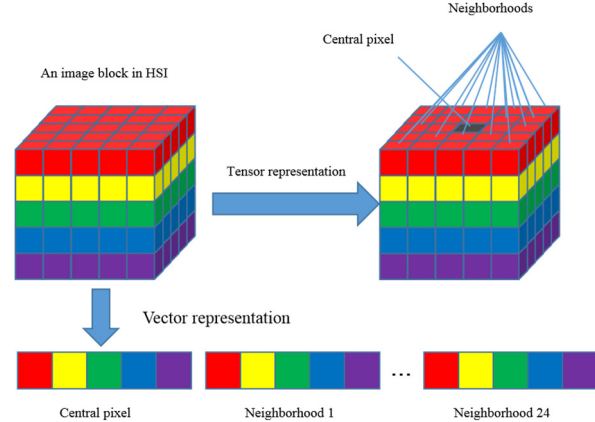


Fig. 2. Difference between tensor and vector representation in HSI data.

tensor A , then tensor A allows rank-R decomposition. Rank-R decomposition can be expressed as

$$\begin{aligned} A &= [[A_1, \dots, A_i, \dots, A_c]] \\ A_c &= [a_c^{(1)}, \dots, a_c^{(i)}, \dots, a_c^{(R)}] \in R^{i_c \times R} \end{aligned} \quad (6)$$

where the symbol $[[\cdot]]$ denotes rank-R decomposition. If the tensor A allows rank-R decomposition, then

$$\begin{aligned} A_{(c)} &= A_c (A_c \odot \dots \odot A_{c+1} \odot A_{c-1} \odot \dots \odot A_1)^T \\ \text{vec}(A) &= (A_c \odot \dots \odot A_1) 1_R \end{aligned} \quad (7)$$

where 1_R represents the rank-1 decomposition of the tensor. For the operation of tensor algebra, refer to [33].

Tensorization: In the hyperspectral target detection method based on tensor representation, it is necessary to construct tensor blocks containing neighborhood information, but HSI pixels are vectors in real space, so HSI pixels need to be tensorize. For the hyperspectral data $A \in R^{i_1 \times i_2 \times i_3}$, i_1 and i_2 represent spatial dimension information, and i_3 represents spectral dimension information. The pixel $a \in R^{i_3}$ can also be expressed as $A_{ii,jj,:} \in R^{i_3}, (1 \leq ii \leq i_1, 1 \leq jj \leq i_2)$. $A_{ii,jj,:}$

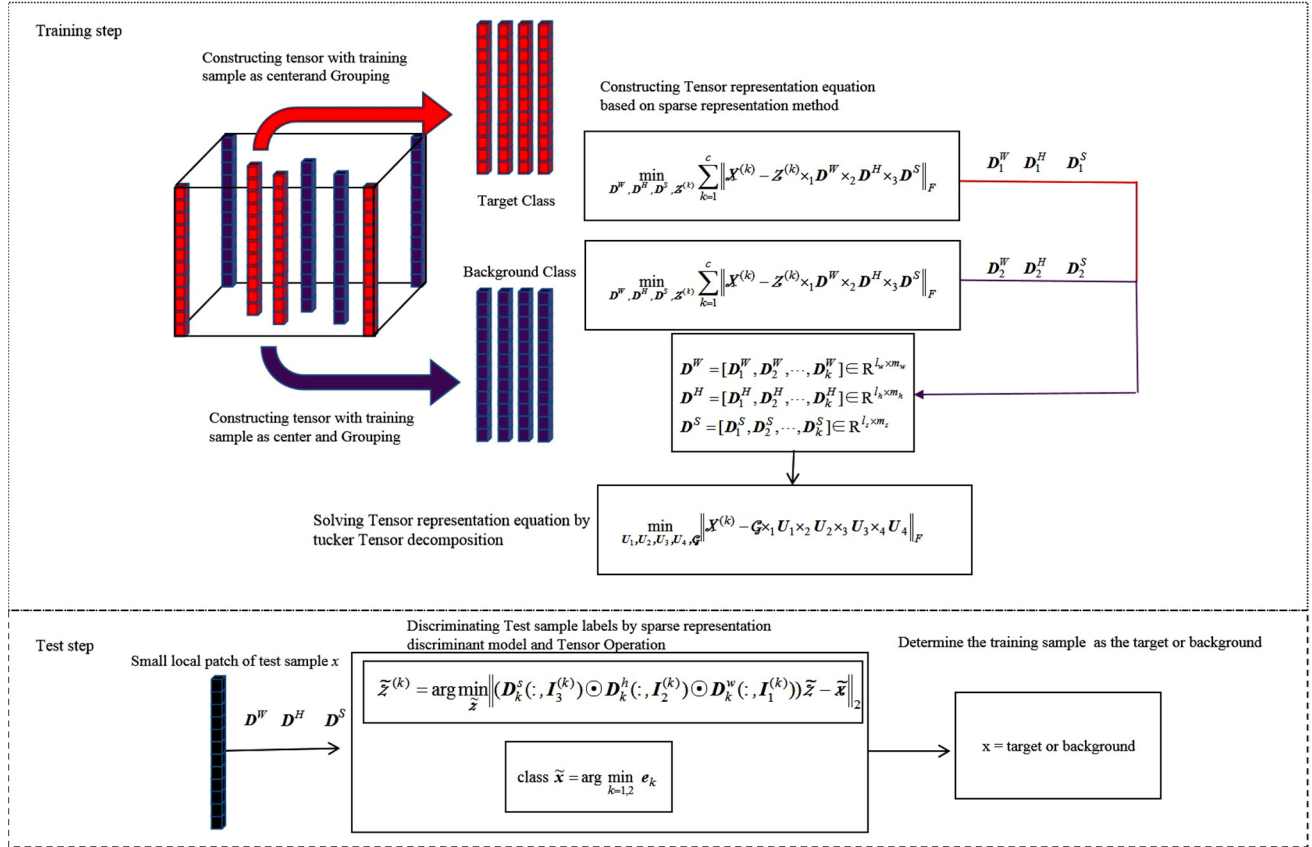


Fig. 3. Overview of hyperspectral target detection method based on nonlocal self-similarity and rank-1 tensor.

becomes a third-order tensor $A' \in R^{n \times n \times i_3}$ after tensorization. The way of tensorization is to add spatial neighborhood information. We use the $n \times n$ circular-shift neighborhood of pixel a to form the tensor vector defined in the $n \times n$ second-order tensor space. More specifically, the formula of tensorization is

$$A'_{w_1, w_2, :} = A_{ii', jj', w_1}, \quad w_2 = 1, 2, \dots, n. \quad (8)$$

When the target spectrum is tensorized, because the target spectrum does not contain spatial information, the target spectrum is selected as its own neighborhood spectrum, and the formula is

$$A'_{w_1, w_2, :} = t w_1, \quad w_2 = 1, 2, \dots, n \quad (9)$$

where $t \in R^{i_3}$ is the target spectrum.

C. Tensor Representation

In recent years, tensor representation is more and more widely used in the field of computer vision and pattern recognition. Compared with vector (first-order tensor) and matrix (second-order tensor), n -order tensor $A \in R^{i_1 \times i_2 \times \dots \times i_n}$ can be defined as n -dimensional array, each order is called n -mode, and a subtensor of a subset can be formed by limiting the value of n . For hyperspectral data $A \in R^{i_1 \times i_2 \times i_3}$, mode-1 and mode-2 represent the spatial dimension information of hyperspectral data, and mode-3 represents spectral dimension information, that is, i_1, i_2 , and i_3 represent the number of rows,

columns, and spectra. The tensor matrix of mode- n is visually illustrated, as shown in Fig. 1.

Based on the tensor algebra principle, HSI can be divided into several image data blocks, and each image block can be processed as a whole. The tensor representation method can make use of the original spatial structure of the image and avoid the loss of spatial constraint information caused by the vector representation method [34]. The visual representation of tensor representation and vector representation is shown in Fig. 2.

III. HYPERSPECTRAL TARGET DETECTION METHOD BASED ON NONLOCAL SELF-SIMILARITY AND RANK-1 TENSOR

In this section, the hyperspectral target detection method based on nonlocal self-similarity and rank-1 tensor is introduced, including the main flow of the algorithm, the calculation of core tensor, and the discrimination of pixels to be tested.

A. Main Flow of the Algorithm

The hyperspectral target detection method based on nonlocal self-similarity and rank-1 tensor uses the nonlocal self-similarity of the image to construct tensor blocks for data processing. Nonlocal self-similarity refers to the repetition of texture and structure of the image, that is, the image blocks in different positions in the image have strong similarity. The structural sparse representation combined with image sparsity

Algorithm: Hyperspectral target detection based on class correlation rank-1 tensor

Require: Dictionaries ($\mathbf{D}^W, \mathbf{D}^H, \mathbf{D}^S$), sparsity level S , test sample \mathbf{x} and its corresponding third-order tensor \mathcal{X} composed of the neighboring pixels

Ensure: Test sample \mathbf{x} is the target or background

1. Set $m = 1, \mathbf{I}_1^k, \mathbf{I}_2^k, \mathbf{I}_3^k = \emptyset, \tilde{\mathcal{Z}}^{(k)} = 0$ and $R_m^k = \mathcal{X}$
2. while $m \leq S$ do
3. $(\mathbf{i}_1^m, \mathbf{i}_2^m, \mathbf{i}_3^m) = \arg \max_{\mathbf{i}_1, \mathbf{i}_2, \mathbf{i}_3} \left| R_m^k \times_1 \mathbf{D}_k^W(:, \mathbf{i}_1)^T \times_2 \mathbf{D}_k^H(:, \mathbf{i}_2)^T \times_3 \mathbf{D}_k^S(:, \mathbf{i}_3)^T \right|$
4. Update the support set $\mathbf{I}_1^k = \mathbf{I}_1^k \cup \mathbf{i}_1^m, \mathbf{I}_2^k = \mathbf{I}_2^k \cup \mathbf{i}_2^m, \mathbf{I}_3^k = \mathbf{I}_3^k \cup \mathbf{i}_3^m, R_m^k = R_m^k - \mathbf{i}_1^m \mathbf{i}_2^m \mathbf{i}_3^m$
5. Identify the vectorized version of $\tilde{\mathcal{Z}}^{(k)}$ by Formula 19
6. Compute the residual E_k by Formula 17
7. $m = m + 1$
8. end while
9. Calculate the norm of the residual e_k by Formula 17
10. Determine the training sample \mathbf{x} as the target or background

Fig. 4. Flow of hyperspectral target detection method based on nonlocal self-similarity and rank-1 tensor.

and nonlocal self-similarity has been successfully applied to different image processing tasks.

The hyperspectral target detection method based on nonlocal self-similarity and rank-1 tensor is mainly divided into two parts. In this step, a number of small patches are extracted from the original HSI. Each patch is a third-order tensor consisting of a training sample located at the center of the patch and several spatial neighborhoods of the training sample. Then, the similar blocks are clustered (the feature similarity of the same category is high), and the sparse representation coefficient is calculated through the target or background dictionary formed by clustering, which is helpful to achieve the sparse representation of blocks and improve the detection performance [35]–[37]. After partitioning and clustering operations, all clustering groups obtained are represented as $\{X_j^k\}_{j=1}^{nk}$, where k represents the k cluster group, nk is the number of blocks in the k cluster, and X_j^k represents the j hyperspectral image block in the k clustering group. The second part is to sparse each hyperspectral image clustering group. Because each group of hyperspectral images is similar in blocks, when the hyperspectral images are divided into blocks for sparse representation, the sparse representation coefficients of each block in the grouping have a similar structure. In the process of block clustering sparse representation of hyperspectral images, each block clustering has a common spatial dictionary \mathbf{D}^W , \mathbf{D}^H and spectral dictionary \mathbf{D}^S . The visual representation of the hyperspectral target detection method based on nonlocal self-similarity and rank-1 tensor is shown in Fig. 3.

B. Calculation of Core Tensor With Nonlocal Self-Similarity

Hyperspectral target detection method based on nonlocal self-similarity and rank-1 tensor can be expressed as

$$\begin{aligned} & \min_{\mathbf{D}^W, \mathbf{D}^H, \mathbf{D}^S, \mathbf{Z}^{(k)}} \sum_{k=1}^c \left\| \mathbf{X}^{(k)} - \mathbf{Z}^{(k)} \times_1 \mathbf{D}^W \times_2 \mathbf{D}^H \times_3 \mathbf{D}^S \right\|_F \\ & \text{s.t. } \|\mathbf{Z}^{(k)}\|_B \leq (r_k^W, r_k^H, r_k^S). \end{aligned} \quad (10)$$

In the formula s.t. $\|\mathbf{Z}^{(k)}\|_B \leq (r_k^W, r_k^H, r_k^S)$ denotes the regularity of the sparsity of tensor blocks, which is used to

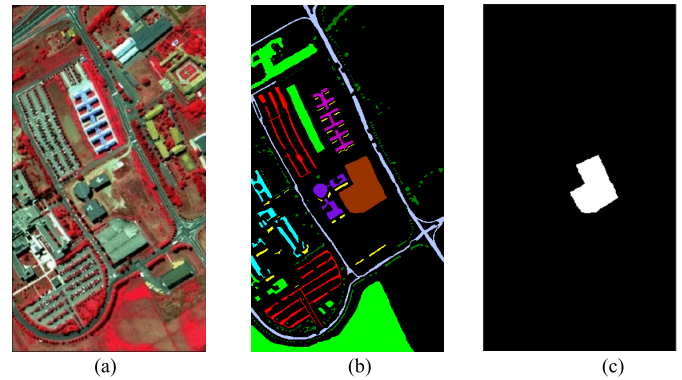


Fig. 5. Pavia University data set. (a) False-color image. (b) Ground truth. (c) Target truth.

ensure the sparsity of the representation coefficient. The spatial and spectral dictionaries of sparse representation are expressed as

$$\begin{aligned} \mathbf{D}^W &= [\mathbf{D}_1^W, \mathbf{D}_2^W, \dots, \mathbf{D}_k^W] \in R^{l_w \times m_w} \\ \mathbf{D}^H &= [\mathbf{D}_1^H, \mathbf{D}_2^H, \dots, \mathbf{D}_k^H] \in R^{l_h \times m_h} \\ \mathbf{D}^S &= [\mathbf{D}_1^S, \mathbf{D}_2^S, \dots, \mathbf{D}_k^S] \in R^{l_s \times m_s}. \end{aligned} \quad (11)$$

Among them, \mathbf{D}_k^W , \mathbf{D}_k^H , and \mathbf{D}_k^S represent the subdictionaries used by each cluster

$m_w = \sum_{k=1}^c r_k^w$, $m_h = \sum_{k=1}^c r_k^h$, $m_s = \sum_{k=1}^c r_k^s$ are the number of atoms in the corresponding dictionary, and r_k^w , r_k^h , and r_k^s are tensor block sparse parameters. Formula (10) can be transformed into a series of small problems, that is, each block clustering $X^{(k)}$ sparse representation of hyperspectral images is only related to class subdictionaries.

Then formula (10) can be expressed as

$$\begin{aligned} & \left\| \mathbf{X}^{(k)} - \mathbf{Z}^{(k)} \times_1 \mathbf{D}^W \times_2 \mathbf{D}^H \times_3 \mathbf{D}^S \right\|_F \\ &= \left\| \mathbf{X}^{(k)} - \text{sub}(\mathbf{Z}^{(k)}) \times_1 \mathbf{D}_k^W \times_2 \mathbf{D}_k^H \times_3 \mathbf{D}_k^S \right\|_F \end{aligned} \quad (12)$$

where $\text{sub}(\mathbf{Z}^{(k)}) \in R^{r_k^W \times r_k^H \times r_k^S \times nk}$ represents the core sub-tensor of $\mathbf{Z}^{(k)}$. Let $\mathbf{Y} = \text{sub}(\mathbf{Z}^{(k)})$, then formula (12) can be

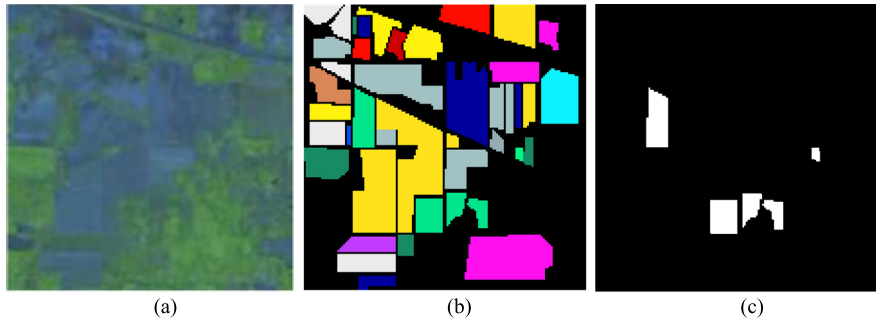


Fig. 6. Indian Pines data set. (a) False-color image. (b) Ground truth. (c) Target truth.

expressed as

$$\min_{\mathbf{D}_k^W, \mathbf{D}_k^H, \mathbf{D}_k^S, \mathbf{Y}} \| \mathbf{X}^{(k)} - \mathbf{Y} \times {}_1\mathbf{D}_k^W \times {}_2\mathbf{D}_k^H \times {}_3\mathbf{D}_k^S \|_F. \quad (13)$$

Through this transformation, the original problem (10) can be transformed into a series of small problems, which makes the problem easier to solve.

If $\mathbf{D}_k^W = {}_1\mathbf{U}_1$, $\mathbf{D}_k^H = {}_2\mathbf{U}_2$, $\mathbf{D}_k^S = {}_3\mathbf{U}_3$, $\mathbf{Y} = \mathbf{G} \times {}_4\mathbf{U}_4$, formula (13) can be expressed as

$$\min_{\mathbf{U}_1, \mathbf{U}_2, \mathbf{U}_3, \mathbf{U}_4, \mathbf{G}} \| \mathbf{X}^{(k)} - \mathbf{G} \times {}_1\mathbf{U}_1 \times {}_2\mathbf{U}_2 \times {}_3\mathbf{U}_3 \times {}_4\mathbf{U}_4 \|_F \quad (14)$$

where the core tensor $\mathbf{G} \in R^{r_k^W \times r_k^H \times r_k^S \times r_k^n}$.

$\mathbf{U}_1 \in R^{l_k^W \times r_k^W}$, $\mathbf{U}_2 \in R^{l_k^H \times r_k^H}$, $\mathbf{U}_3 \in R^{l_k^S \times r_k^S}$, $\mathbf{U}_4 \in R^{n_k \times r_k^n}$ represent the base vectors. Formula (14) can be solved by Tucker decomposition, from which the solution of formula (13) is determined.

For the detection of pixel \tilde{x} to be tested, in order to make full use of the label information of its neighborhood tensor block, this article uses the target dictionary and background dictionary to constrain the structural sparsity of the core tensor $\tilde{\mathbf{Z}}^{(k)}$

$$\begin{aligned} & \min_{\tilde{\mathbf{Z}}^{(k)}} \| \tilde{\mathbf{X}} - \tilde{\mathbf{Z}}^{(k)} \times {}_1\mathbf{D}_k^W \times {}_2\mathbf{D}_k^H \times {}_3\mathbf{D}_k^S \|_F \\ & \text{s.t. } \|\tilde{\mathbf{Z}}^{(k)}\|_B \leq (\tilde{r}_k^W, \tilde{r}_k^H, \tilde{r}_k^S). \end{aligned} \quad (15)$$

The core tensor $\tilde{\mathbf{Z}}^{(k)}$ can be solved by formula (15).

C. Discrimination of Pixel With Rank-1 Tensor Operation

Same as the sparse representation method, then it can be determined that the pixel \tilde{x} to be tested belongs to the target or background according to the minimum residual

$$\text{class } \tilde{x} = \operatorname{argmin}_{k=1,2} e_k \quad (16)$$

where

$$\begin{aligned} e_k &= \|\operatorname{vec}(\mathbf{E}_k)\|_2 \\ \mathbf{E}_k &= \tilde{\mathbf{X}} - \tilde{\mathbf{Z}}^{(k)} \left(\mathbf{I}_1^{(k)}, \mathbf{I}_2^{(k)}, \mathbf{I}_3^{(k)} \right) \\ &\quad \times {}_1\mathbf{D}_k^W \left(:, \mathbf{I}_1^{(k)} \right) \times {}_2\mathbf{D}_k^H \left(:, \mathbf{I}_2^{(k)} \right) \times {}_3\mathbf{D}_k^S \left(:, \mathbf{I}_3^{(k)} \right) \end{aligned} \quad (17)$$

$\operatorname{vec}(\cdot)$ denotes the vectorization of the tensor, \mathbf{I}_1^k , \mathbf{I}_2^k , \mathbf{I}_3^k is the support set of the core tensor $\tilde{\mathbf{Z}}^{(k)}$. Making full use of the sparsity between tensor blocks of the same class is helpful to

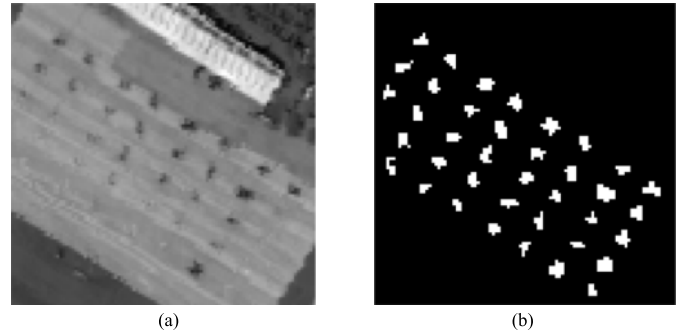


Fig. 7. San Diego data set. (a) Grayscale map. (b) Target truth.

improve the detection rate of the detector. Assuming that the test sample $\tilde{\mathbf{X}}$ examples belongs to the target class, several atoms in the target dictionary (\mathbf{D}_t^w , \mathbf{D}_t^h , \mathbf{D}_t^s) can accurately represent the test sample $\tilde{\mathbf{X}}$, while more atoms from the background dictionary (\mathbf{D}_b^w , \mathbf{D}_b^h , \mathbf{D}_b^s) are required to represent the test sample $\tilde{\mathbf{X}}$ with the same accuracy. Under certain sparse constraints, the error of the $\tilde{\mathbf{X}}$ as a target will be smaller. Therefore, the support set \mathbf{I}_1^k , \mathbf{I}_2^k , \mathbf{I}_3^k in formula 17 can make better use of the sparsity between tensor blocks. Simply, the support set \mathbf{I}_1^k , \mathbf{I}_2^k , \mathbf{I}_3^k is the index that represents the target dictionary or background dictionary.

The rank-1 regular decomposition Kronecker product of core tensor $\tilde{\mathbf{z}}^{(k)}$ can be expressed as the following:

$$\begin{aligned} \tilde{\mathbf{z}}^{(k)} &= \operatorname{argmin}_{\tilde{\mathbf{z}}} \| \left(\mathbf{D}_k^s \left(:, \mathbf{I}_3^{(k)} \right) \right. \\ &\quad \left. \otimes \mathbf{D}_k^h \left(:, \mathbf{I}_2^{(k)} \right) \otimes \mathbf{D}_k^w \left(:, \mathbf{I}_1^{(k)} \right) \right) \tilde{\mathbf{z}} - \tilde{\mathbf{x}} \|_2. \end{aligned} \quad (18)$$

According to the tensor algebra operation in Section II, formula (18) can be transformed into the expression of Khatri–Rao product

$$\begin{aligned} \tilde{\mathbf{z}}^{(k)} &= \operatorname{argmin}_{\tilde{\mathbf{z}}} \| \left(\mathbf{D}_k^s \left(:, \mathbf{I}_3^{(k)} \right) \right. \\ &\quad \left. \odot \mathbf{D}_k^h \left(:, \mathbf{I}_2^{(k)} \right) \odot \mathbf{D}_k^w \left(:, \mathbf{I}_1^{(k)} \right) \right) \tilde{\mathbf{z}} - \tilde{\mathbf{x}} \|_2. \end{aligned} \quad (19)$$

As shown in Fig. 4, the algorithm flow proposed in this article uses the tensor algebra operation of rank-1 canonical decomposition of weights to apply the spatial and spectral information of hyperspectral tensors to hyperspectral target detection.

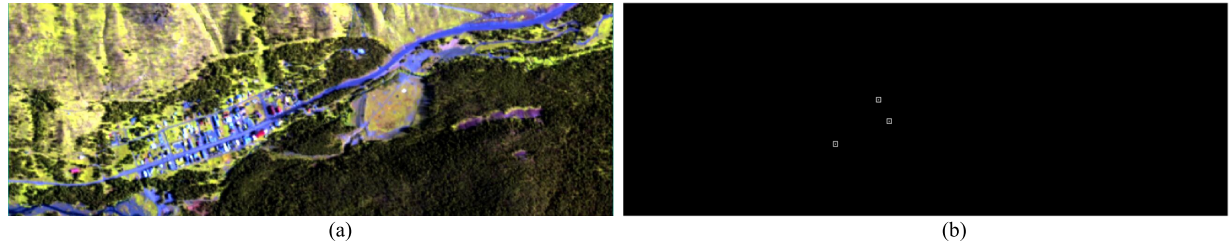


Fig. 8. HyMap data set. (a) Color image. (b) Target truth.

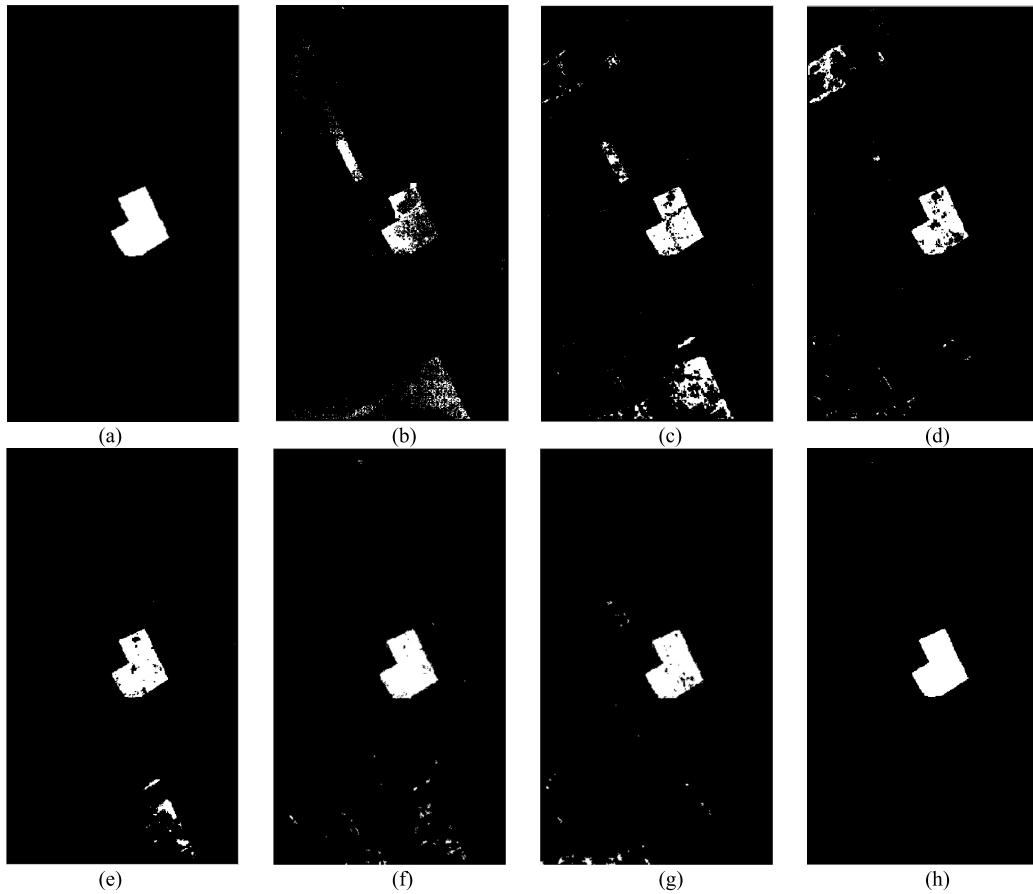


Fig. 9. Detection results obtained by (a) target truth, (b) OSP, (c) TACE, (d) LCRD, (e) plSRC, (f) MultiRely, (g) Sparse-Spatial CEM, and (h) TBDL.

TABLE I
RUN TIME OF EACH ALGORITHM

	OSP	TACE	LCRD	plSRC	MultiRely	Sparse-SpatialCEM	TBDL
Pavia University Completion time(s)	5.53	6.42	51.61	80.54	185.47	82.74	341.23
Indian Pines Completion time(s)	3.89	5.07	32.54	32.56	137.56	76.32	261.25
San Diego Completion time(s)	1.12	3.68	32.58	47.74	105.36	63.59	163.26

Hyperspectral images contain second-order spatial information and first-order spectral information. At the same time, tensors can also contain third-order information. Therefore, in the tensor representation theory, the third-order tensor can be used to maintain the 3-D spatial structure of hyperspectral data. The third-order tensor can contain not only the second-order spatial information, but also the first-order spectral

information. The characteristics of the tensor are consistent with those of the hyperspectral data, which is a physical explanation that tensor is helpful to target detection [38]–[40].

In particular, the dimension of the hyperspectral tensor is decomposed into a spatial dictionary and a spectral dictionary, which provides a quantitative representation of the target detection performance of each dimension. To put it more

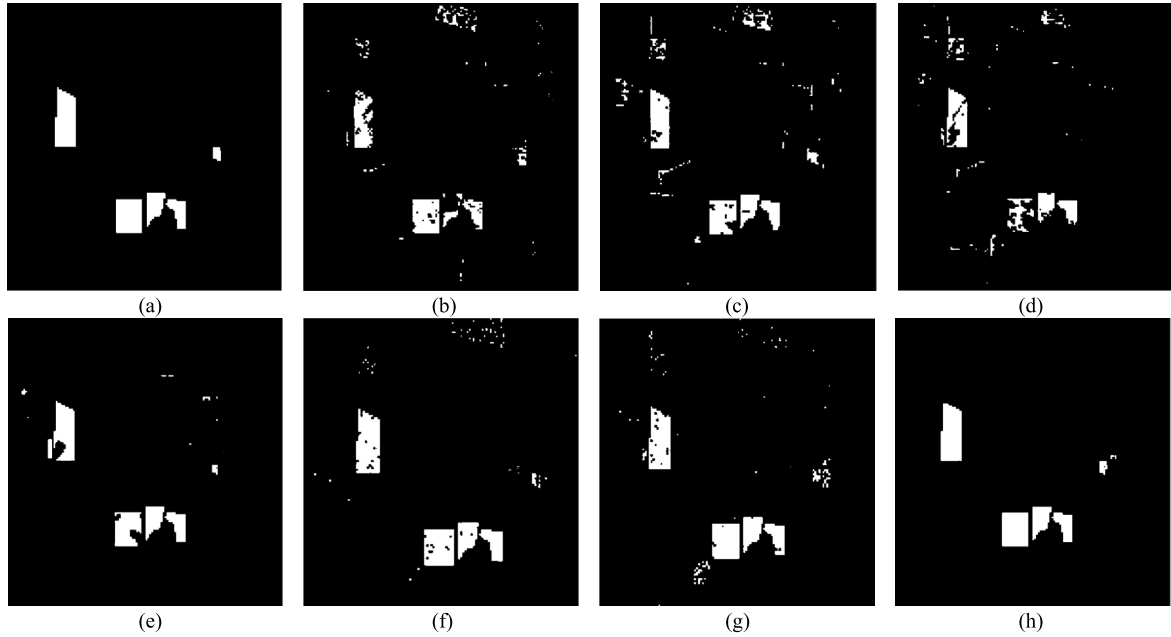


Fig. 10. Detection results obtained by (a) target truth, (b) OSP, (c) TACE, (d) LCRD, (e) plSRC, (f) MultiRely, (g) Sparse-SpatialCEM, and (h) TBDL.

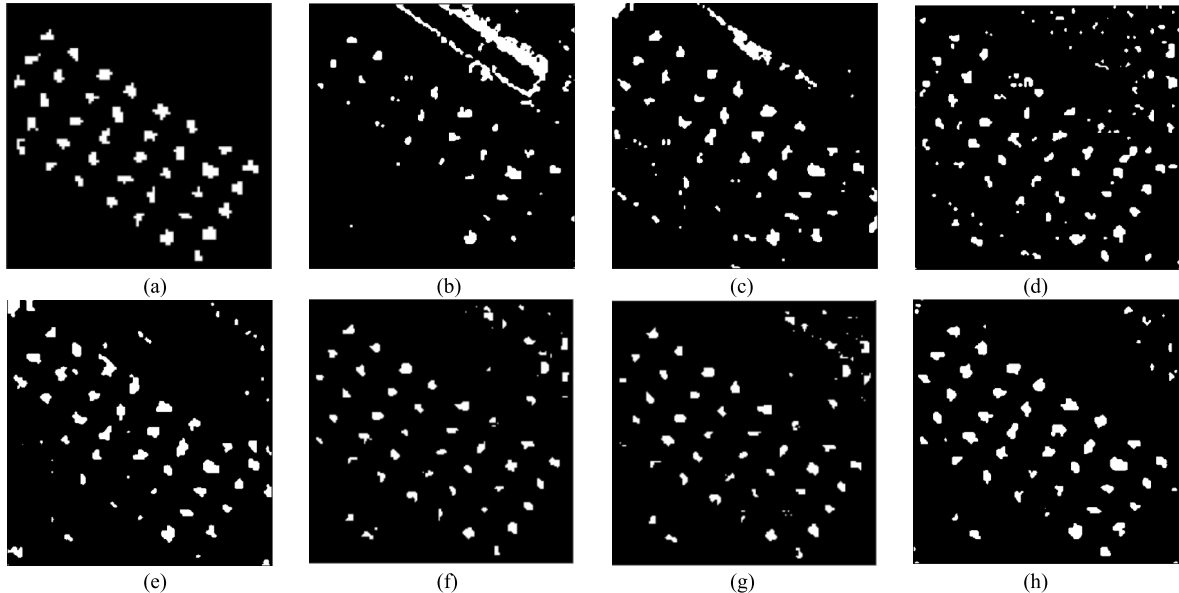


Fig. 11. Detection results obtained by (a) target truth, (b) OSP, (c) TACE, (d) LCRD, (e) plSRC, (f) MultiRely, (g) Sparse-SpatialCEM, and (h) TBDL.

simply, the spatial dictionaries D^w and D^h are used to represent the spatial similarity of each category, and the spectral dictionary D^s is used to represent the spectral bands of each category. The method proposed in this article quantifies the importance of spectrum for hyperspectral data and promotes the physical interpretation of hyperspectral data analysis.

IV. EXPERIMENTAL SECTION

In this section, four real HSI data sets are used for experiments and the proposed method is compared with six commonly used algorithms to evaluate its effectiveness. These compared methods include classical orthogonal subspace projection (OSP), the detector based on cooperative representation

(LCRD) [41], the detection method which used spectral features extracted by 3-D sparse tensor and combined with ACE detector as target detection (TACE) [42], an improved block-based SRC with spatial smoothing and spectral dictionary is constructed (plSRC) [43], the detection method of multi-task learning and target reliability analysis (MultiRely) [8], and the sparsity and spatial correlation constraint detection algorithm (Sparse-SpatialCEM) [44].

A. Introduction for Experimental Data Sets

The experimental data using Pavia University, Indian Pines, San Diego Airport, and HyMap have different remote sensing

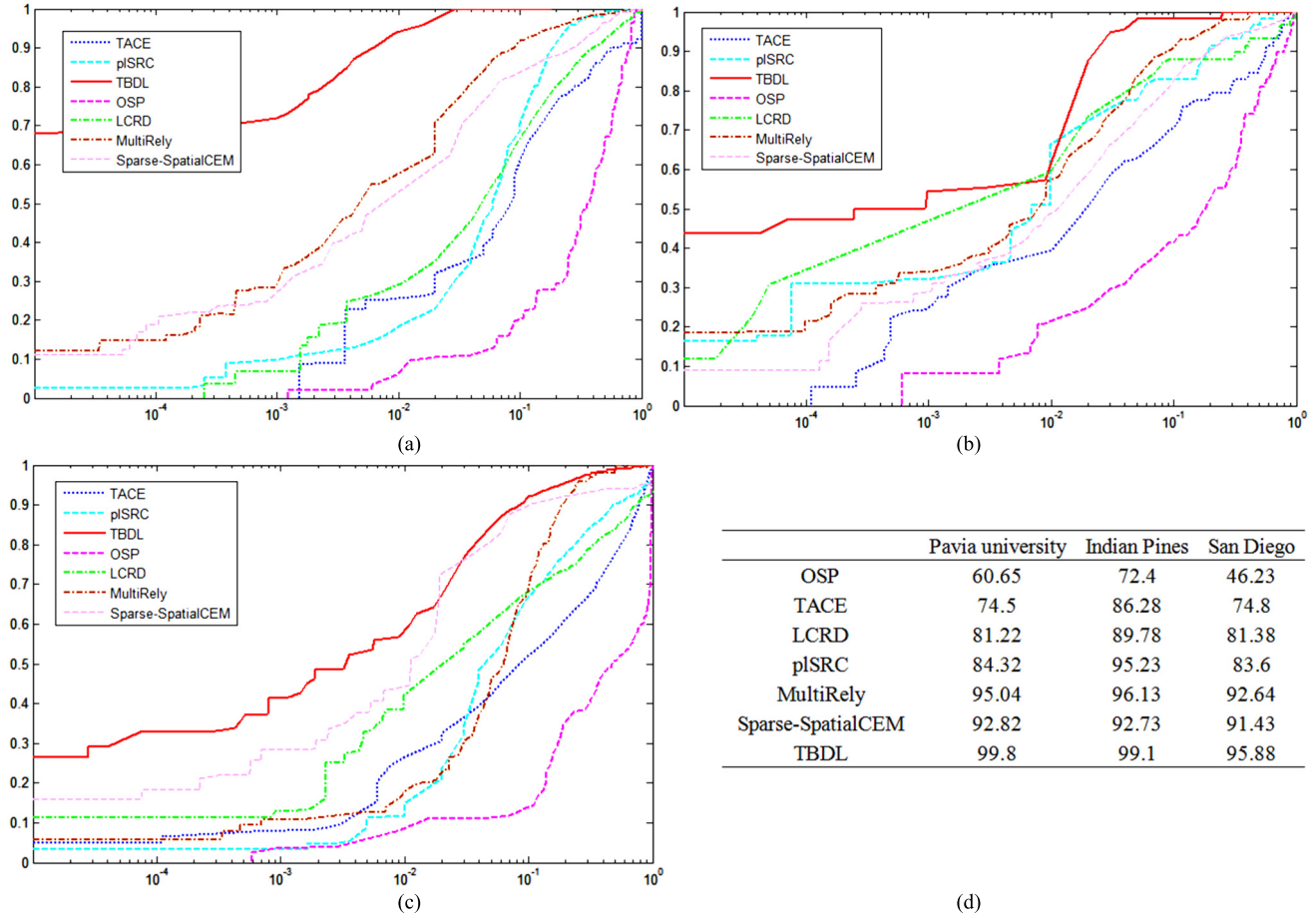


Fig. 12. Roc curves of (a) Pavia University, (b) Indian Pines, (c) San Diego, and (d) AUC values of each experiment.

environment and spatial resolution, which can better reflect the detection effect. Additionally, there are many related researches on these four data sets, which have strong versatility [4], [45], [46]. The Pavia University, Indian Pines, and San Diego Airport data sets were used in the first evaluation experiment and the Hymap data set for the second evaluation experiment. The details of these data sets are introduced respectively as follows.

Pavia University: The first experimental image is the real hyperspectral data of Pavia University collected by the spectrometer ROSIS, with a wavelength range of 0.43–0.86 μm . After removing the bands affected by water absorption and noise, it has 103 available bands with a spatial resolution of 1.3m. The spatial pixel size of the original image data is 610×340 , as shown in Fig. 5(a). The real feature distribution is shown in Fig. 5(b). Pavia University consists of nine types of features, of which type 6 Bare Soil is selected as the target and the rest as the background, as shown in Fig. 5(c).

Indian Pines: The second experimental image is a hyperspectral image obtained from a farm in Indiana, USA, collected by an AVIRIS sensor with a wavelength range of 0.4–2.5 μm . After removing the bands affected by water absorption and noise, the second experimental image has 220 available bands with a spatial resolution of 20 m. The spatial pixel size of the original image data is 145×145 . Fig. 6(a) and (b)

shows a false-color image of Indian Pines data and a real figure distribution map. The image contains 16 types of land cover, and type 6 grass-trees are selected as the detection target, as shown in Fig. 6(c).

San Diego: The third experimental image is the real hyperspectral data of San Diego area collected by AVIRIS sensor. The wavelength range is 0.4–1.8 μm . After removing the bands affected by water absorption and noise, the third experimental image has 126 available bands, the spatial resolution is 3.5 m, and the spatial pixel size of the original image data is 400×400 . The data of the airport part are intercepted as the real hyperspectral experimental data, and the spatial pixel size is 100×100 . The captured image is shown in Fig. 7(a), and the real figure distribution is shown in Fig. 7(b).

HyMap: The fourth experimental image is the real hyperspectral data of Cook Town area collected by HyMap sensor. The wavelength range is 0.45–2.5 μm . After removing the bands affected by water absorption and noise, the fourth experimental image has 124 available bands with a spatial resolution of 3m. The spatial pixel size of the original image data is 280×800 . This article tests three-vehicle targets in the HyMap image called V1, V2, and V3 respectively. Fig. 8(a) is the false-color images of the HyMap data and Fig. 8(b) is the target ground truth maps. Among them, there are two different

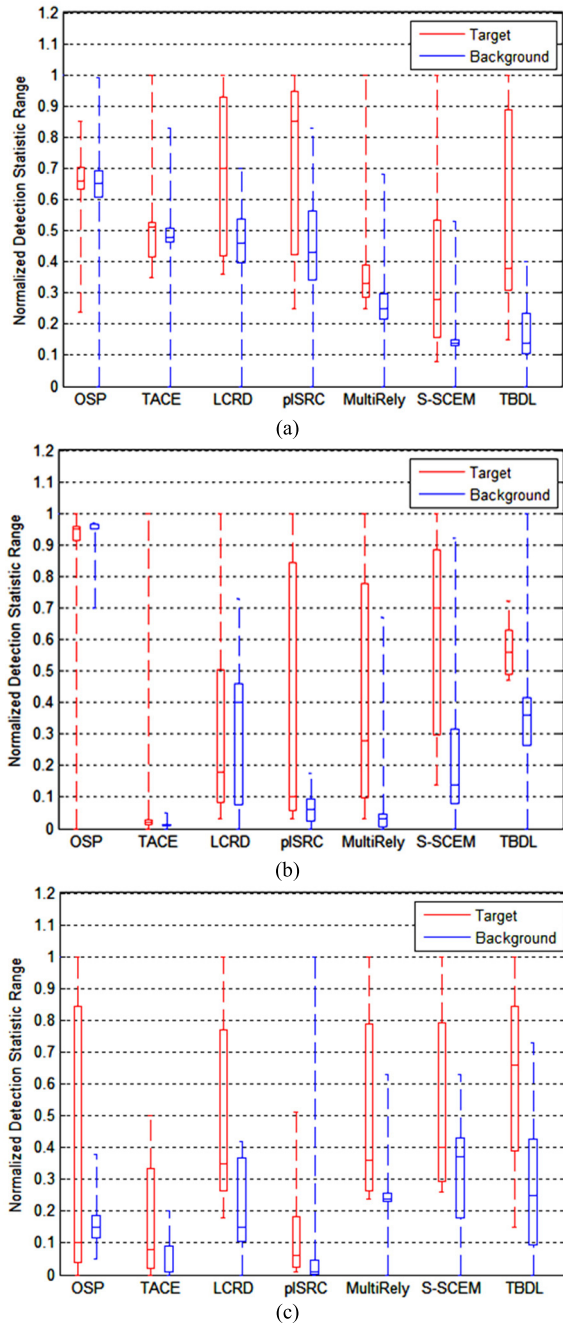


Fig. 13. Separability map. (a) Pavia University. (b) Indian Pines. (c) San Diego.

spectral characteristics of V2. This article uses paint features of white trucks.

B. Compared Methods and Experimental Settings

In order to verify the performance of the algorithm, this article compares it with six common algorithms, including OSP, TACE, LCRD, pISRC, MultiRely, and Sparse-SpatialCEM. The OSP uses spectral information as a vector and projects it into an orthogonal subspace for target detection. The LCRD is based on collaborative representation, the pISRC is based on sparse spectral dictionary, the LCRD and the pISRC are based on sparse representation using spectral-spatial information



Fig. 14. AUC of (a) Pavia University, (b) Indian Pines, and (c) San Diego.

combination. The TACE method based on 3-D sparse tensor, but it takes the input data as a vector and ignores the 3-D spatial structure of the HSI. The MultiRely method combines multitask learning and target reliability analysis. The Sparse-SpatialCEM method combines sparse and spatial correlation on the basis of CEM detector. These comparison methods are widely used in the field of target detection and have been cited in many articles [47]–[50].

In the experiment, 5% of the samples were randomly selected as training samples and the rest as test samples. The experiment was conducted with MATLAB on the platform of the Windows 7 operating system. The LCRD parameter is set to the regularization parameter $\lambda = 10^{-6}$, the outer

TABLE II
SCORES AND FALSE ALARM RATES OF DIFFERENT ALGORITHMS FOR THE HYMAP SET

Target	OSP	TACE	LCRD	pISRC	MultiRely	Sparse-Spatial CEM	TBDL
V1	57445 (0.25645)	8250 (0.03680)	5773 (0.02566)	8660 (0.03863)	4420 (0.01976)	7973 (0.03561)	3206 (0.01430)
	93219 (0.41615)	2685 (0.01195)	14042 (0.06266)	2240 (0.01001)	55370 (0.24717)	111215 (0.49651)	2124 (0.00949)
V2	120320 (0.53712)	20742 (0.09260)	2130 (0.00951)	27345 (0.12208)	2860 (0.01275)	4061 (0.01813)	2864 (0.01279)

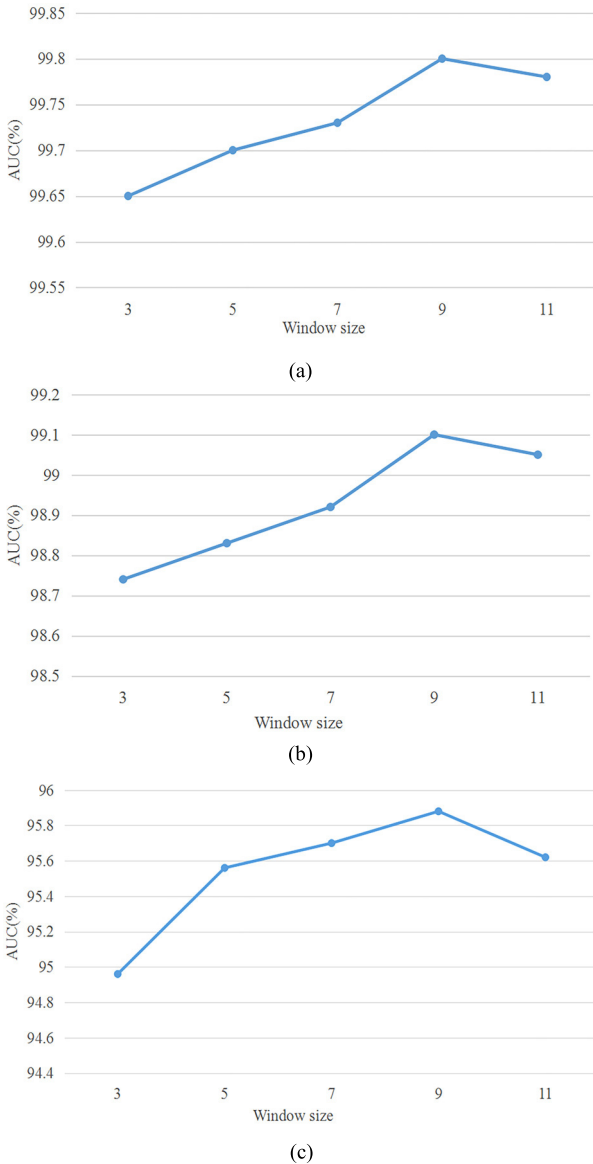


Fig. 15. AUC versus the size of spatial window. (a) Pavia University. (b) Indian Pines. (c) San Diego.

window size is 13, and the inner window size is 7. The neighborhood size of the pISRC is set to 7×7 . In the TACE method, the regularization parameter $\lambda = 20$, $\tau = 1$, the decomposition rank is $(0.8I_1 \sim 0.8I_2 \sim 10)$, where I_1 and

I_2 are the height and width of the image. The tensor block size of the TBDL is set to 9×9 , and the sparsity $S = 100$. In the MultiRely method, the task number $K = 5$, signal-noise ratio $SNR = 3$. In the Sparse-SpatialCEM method, the limiting case $\mu = 0.7$, parameter $\rho_1 = \rho_2 = 0.4$. Different methods set neighborhood windows of different sizes, but this setting optimizes the detection performance of these methods, and it is more reasonable to compare these methods in the case of optimal performance.

In order to better test the effectiveness of the TBDL algorithm, this article uses two evaluation methods. For the three data sets of Pavia University, Indian Pines, and San Diego, the evaluation used receiver operating characteristic (ROC) and area under curve (AUC), which are commonly used in the field of hyperspectral image processing [10], [51]–[54]. For the HyMap data set, the online scoring application provided by the RIT website is used [55], [56]. The score represents the number of false alarms detected when targets are detected, detecting numbers of pixels larger than or equal to target location pixels. Obviously, the smaller score, the better detection effect.

C. First Evaluation of the TBDL Method

Figs. 9–11 show the detection results of three HSI data sets, respectively. Fig. 12 shows the ROC curves and AUC values of three HSI data sets. In Fig. 13, the red and blue boxes represent the distribution of 80% of the data in the middle of the target and background, the largest 10% and the smallest 10% are removed, and the horizontal lines in the box represent the data mean [57]–[59]. According to the experimental results, the following discussions are made in this experiment.

The test results of the OSP and TACE are more loose, and there are more errors. In the visual detection results of the LCRD, pISRC, MultiRely, Sparse-SpatialCEM, and TBDL, the background is cleaner and the detection errors are more concentrated in space. This is mainly due to the fact that the OSP and the TACE only use the spectral information of the HSI and the combination of spectral–spatial information of the LCRD, pISRC, MultiRely, Sparse-SpatialCEM, and TBDL. As shown in the ROC curve of Fig. 12, the method based on the combination of spectral and spatial information provides better detection results. This verifies the advantage of HSI spatial information for target detection.

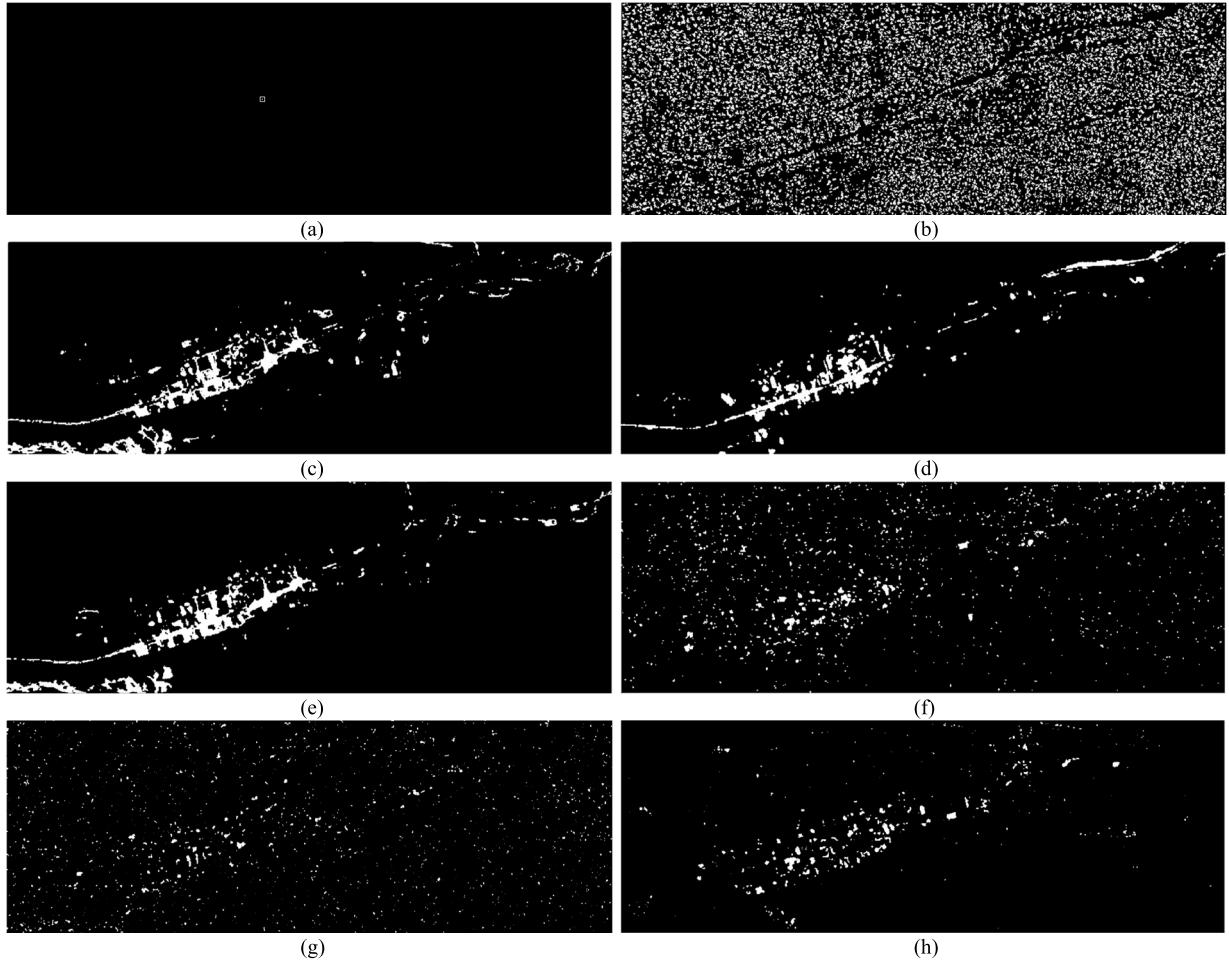


Fig. 16. Detection results obtained by (a) target truth, (b) OSP, (c) TACE, (d) LCRD, (e) plSRC, (f) MultiRely, (g) Sparse-SpatialCEM, and (h) TBDL.

Compared with the classical OSP detector, the TACE, which uses tensor to represent spectral information and combines ACE detector, can improve the target detection effect, although the improvement is limited. This is mainly due to the fact that the TACE uses the 3-D sparse tensor representation of HSI on the basis of only spectral information. This verifies that the tensor representation method is helpful to improve the effect of target detection when using spectral information for target detection.

In the method of sparse representation, the plSRC and the MultiRely have better detection effect than the LCRD. This is mainly due to the fact that the plSRC and the MultiRely use the dictionary learning method to represent test samples more effectively. As shown in Figs. 9–11, it is proved that the sparse representation method based on dictionary learning is more effective in target detection.

Target detection methods based on tensor representation or using spatial information (TACE and TBDL) have better detection results than those based on sparse representation or using spectral information (OSP, LCRD, plSRC, MultiRely, and Sparse-SpatialCEM). All the methods mentioned, the TBDL provides the best test results. As shown in Figs. 9–11, the TBDL is closer to the true value of the ground than other methods.

Among the TBDL experimental results of the three HSI data sets, the detection effect of Pavia University data is the best and the improvement of San Diego data is the least. If the difference between environment and band is ignored, this is mainly because the detection effect of the TBDL is better for centralized targets. If the target area is very narrow or loose, the target detection effect of this kind of target will be poor. This is also reflected in the Indian Pines data set, and the detection effect of the narrow area on the far right in Fig. 10(h) is also not as better as that of other regions. This is the main problem to be solved in the next step of this research.

The method proposed in this article uses the tensor representation to represent the hyperspectral data, maintains the spatial structure of the hyperspectral data, and uses the spatial correlation between pixels to improve the target detection performance. In particular, the use of spatial correlation can significantly improve the detection effect of target or background focus areas, so in Figs 9, 10, and 11, the background is purer and the false alarm rate is lower.

Table I shows the running time of each algorithm. The time of TBDL is a little longer, but not more than 5 minutes. The most important calculation of TBDL includes the calculation of core tensor and residual, and its computational complexity is $O(s^3 + s^3d)$, where s represents the number of bands and d

represents the number of dictionary atoms. Therefore, tensor operation does not consume too much computing time, but it takes more time in the process of block sparse representation.

D. Parameter Analysis of the TBDL Method

In this section, it compares the detection results of different algorithms on three HSI data sets under different percentages of training samples. Moreover, the relationship between window size and AUC is discussed.

The AUC values of different methods are shown in Fig. 13 when the percentage of training sample is 0.5%, 1%, 2%, 3%, 4%, 5%, and the AUC values of different methods are shown in Fig. 14. Choose different window sizes, and the AUC value of the TBDL with different window sizes is shown in Fig. 15.

This experiment has the following discussion.

The more the number of training samples, the better the effect of target detection. When the number of training samples is 0.5%, TBDL can achieve better results in three HSI data sets. When the number of training samples is 5%, the AUC value is greater than 90%.

In the Indian Pines data set of the three HSI data sets, even if a small number of training samples are selected, the detection results of each method are better. When the training sample is greater than 2%, the AUC value of each method is more than 80%, except the OSP. However, the TBDL still has a promising performance even when the number of training samples is small.

Fig. 15 shows that the selection of different window sizes has little effect on the detection results. On the three HSI data sets, the fluctuation of AUC is not more than 1%. But this can show a decreasing trend, that is, when the window is selected too small, the spatial information is not enough to achieve a better detection effect. When the window selection is too large, it may contain pixels of different features, thus reducing the detection effect.

E. Second Evaluation of the TBDL Method

In this section, this article uses the score of HyMap data set to verify the performance of the TBDL.

Table II shows scores and false alarm rates of different algorithms (false alarm rate in parentheses). To show the results visually, the target detection results for V1 are plotted in Fig. 16. Experimental results show that the TBDL has the best performance in detection results for three targets V1, V2, and V3. According to scores given in Table II, none of these algorithms has the best detection results for all targets, but the overall performance of the TBDL is better than those of others. Therefore, it can be concluded that the TBDL performs better than other compared algorithms on the HyMap data set.

To sum up, through the detection results, it is proved that the TBDL can improve the performance of target detection.

V. CONCLUSION

In this article, a hyperspectral target detection method based on nonlocal self-similar and rank-1 tensor is proposed.

Specifically, as the third-order tensor is used as the input of the proposed method to preserve the spatial information of HSI data, which solves the problem of the loss of HSI data structure in the vectorization process used in the traditional methods. In addition, by taking advantage of the tensor algebra principle and rank-1 canonical decomposition attribute, the tensor operation process is simplified, and better detection results can be obtained with fewer training samples. As far as we know, the application of tensor rank-1 regular decomposition attribute in sparse representation is considered for the first time in the proposed method. In the future, other tensor algebraic operation methods and hyperspectral data characteristics will be considered to provide more accurate analysis for remote sensing applications.

REFERENCES

- [1] W. Xie, J. Lei, J. Yang, Y. Li, Q. Du, and Z. Li, "Deep latent spectral representation learning-based hyperspectral band selection for target detection," *IEEE Trans. Geosci. Remote Sens.*, vol. 58, no. 3, pp. 2015–2026, Mar. 2020.
- [2] W. Guo, W. Yang, H. Zhang, and G. Hua, "Geospatial object detection in high resolution satellite images based on multi-scale convolutional neural network," *Remote Sens.*, vol. 10, no. 1, p. 131, Jan. 2018.
- [3] L. He, J. Li, C. Liu, and S. Li, "Recent advances on spectral–spatial hyperspectral image classification: An overview and new guidelines," *IEEE Trans. Geosci. Remote Sens.*, vol. 56, no. 3, pp. 1579–1597, Mar. 2018.
- [4] X. Lu, W. Zhang, and X. Li, "A hybrid sparsity and distance-based discrimination detector for hyperspectral images," *IEEE Trans. Geosci. Remote Sens.*, vol. 56, no. 3, pp. 1704–1717, Mar. 2018.
- [5] W. Xie, Y. Li, W. Zhou, and Y. Zheng, "Efficient coarse-to-fine spectral rectification for hyperspectral image," *Neurocomputing*, vol. 275, pp. 2490–2504, Jan. 2018.
- [6] Y. Li, W. Xie, and H. Li, "Hyperspectral image reconstruction by deep convolutional neural network for classification," *Pattern Recognit.*, vol. 63, pp. 371–383, Mar. 2017.
- [7] C. Jiao, C. Chen, R. G. McGarvey, S. Bohlman, L. Jiao, and A. Zare, "Multiple instance hybrid estimator for hyperspectral target characterization and sub-pixel target detection," *ISPRS J. Photogramm. Remote Sens.*, vol. 146, pp. 235–250, Dec. 2018.
- [8] Y. Zhang, K. Wu, B. Du, and X. Hu, "Multitask learning-based reliability analysis for hyperspectral target detection," *IEEE J. Sel. Topics Appl. Earth Observ. Remote Sens.*, vol. 12, no. 7, pp. 2135–2147, Jul. 2019.
- [9] C.-I. Chang, "Statistical detection theory approach to hyperspectral image classification," *IEEE Trans. Geosci. Remote Sens.*, vol. 57, no. 4, pp. 2057–2074, Apr. 2019.
- [10] L. Wang *et al.*, "Band subset selection for anomaly detection in hyperspectral imagery," *IEEE Trans. Geosci. Remote Sens.*, vol. 55, no. 9, pp. 4887–4898, Sep. 2017.
- [11] S. Matteoli, M. Diani, and G. Corsini, "Closed-form nonparametric GLRT detector for subpixel targets in hyperspectral images," *IEEE Trans. Aerosp. Electron. Syst.*, vol. 56, no. 2, pp. 1568–1581, Apr. 2020.
- [12] D. Zhu, B. Du, and L. Zhang, "Target dictionary construction-based sparse representation hyperspectral target detection methods," *IEEE J. Sel. Topics Appl. Earth Observ. Remote Sens.*, vol. 12, no. 4, pp. 1254–1264, Apr. 2019.
- [13] W. Xie, Y. Shi, Y. Li, X. Jia, and J. Lei, "High-quality spectral-spatial reconstruction using saliency detection and deep feature enhancement," *Pattern Recognit.*, vol. 88, pp. 139–152, Apr. 2019.
- [14] S. Rambhatla, X. Li, J. Ren, and J. Haupt, "A dictionary-based generalization of robust PCA with applications to target localization in hyperspectral imaging," *IEEE Trans. Signal Process.*, vol. 68, pp. 1760–1775, Mar. 2020.
- [15] Y. Ren, L. Liao, S. J. Maybank, Y. Zhang, and X. Liu, "Hyperspectral image spectral-spatial feature extraction via tensor principal component analysis," *IEEE Geosci. Remote Sens. Lett.*, vol. 14, no. 9, pp. 1431–1435, Sep. 2017.

- [16] Y. Liu, G. Gao, and Y. Gu, "Tensor matched subspace detector for hyperspectral target detection," *IEEE Trans. Geosci. Remote Sens.*, vol. 55, no. 4, pp. 1967–1974, Apr. 2017.
- [17] H. Zhai, H. Zhang, L. Zhang, and P. Li, "Laplacian-regularized low-rank subspace clustering for hyperspectral image band selection," *IEEE Trans. Geosci. Remote Sens.*, vol. 57, no. 3, pp. 1723–1740, Mar. 2019.
- [18] L. Zhang, L. Zhang, D. Tao, X. Huang, and B. Du, "Hyperspectral remote sensing image subpixel target detection based on supervised metric learning," *IEEE Trans. Geosci. Remote Sens.*, vol. 52, no. 8, pp. 4955–4965, Aug. 2014.
- [19] X. Kang, X. Zhang, S. Li, K. Li, J. Li, and J. A. Benediktsson, "Hyperspectral anomaly detection with attribute and edge-preserving filters," *IEEE Trans. Geosci. Remote Sens.*, vol. 55, no. 10, pp. 5600–5611, Oct. 2017.
- [20] H. Zhang, Y. Li, Y. Jiang, P. Wang, Q. Shen, and C. Shen, "Hyperspectral classification based on lightweight 3-D-CNN with transfer learning," *IEEE Trans. Geosci. Remote Sens.*, vol. 57, no. 8, pp. 5813–5828, Aug. 2019.
- [21] Q. Wang, F. Zhang, and X. Li, "Optimal clustering framework for hyperspectral band selection," *IEEE Trans. Geosci. Remote Sens.*, vol. 56, no. 10, pp. 5910–5922, Oct. 2018.
- [22] X. Cao, T. Xiong, and L. Jiao, "Supervised band selection using local spatial information for hyperspectral image," *IEEE Geosci. Remote Sens. Lett.*, vol. 13, no. 3, pp. 329–333, Mar. 2016.
- [23] H. E. Motteler and L. L. Strow, "AIRS deconvolution and the translation of AIRS-to-CrIS radiances with applications for the IR climate record," *IEEE Trans. Geosci. Remote Sens.*, vol. 57, no. 3, pp. 1793–1803, Mar. 2019.
- [24] Y. Zhan, D. Hu, H. Xing, and X. Yu, "Hyperspectral band selection based on deep convolutional neural network and distance density," *IEEE Geosci. Remote Sens. Lett.*, vol. 14, no. 12, pp. 2365–2369, Dec. 2017.
- [25] L. Xiao, Y. Liu, T. Huang, X. Liu, and X. Wang, "Distributed target detection with partial observation," *IEEE Trans. Signal Process.*, vol. 66, no. 6, pp. 1551–1565, Mar. 2018.
- [26] C. Zhao and L. Zhang, "Spectral-spatial stacked autoencoders based on low-rank and sparse matrix decomposition for hyperspectral anomaly detection," *Infr. Phys. Technol.*, vol. 92, pp. 166–176, Aug. 2018.
- [27] Y. Su, J. Li, A. Plaza, A. Marinoni, P. Gamba, and S. Chakravortty, "DAEN: Deep autoencoder networks for hyperspectral unmixing," *IEEE Trans. Geosci. Remote Sens.*, vol. 57, no. 7, pp. 4309–4321, Jul. 2019.
- [28] Y. Wang, J. Peng, Q. Zhao, Y. Leung, X.-L. Zhao, and D. Meng, "Hyperspectral image restoration via total variation regularized low-rank tensor decomposition," *IEEE J. Sel. Topics Appl. Earth Observ. Remote Sens.*, vol. 11, no. 4, pp. 1227–1243, Apr. 2018.
- [29] Z. Wang, N. M. Nasrabadi, and T. S. Huang, "Spatial-spectral classification of hyperspectral images using discriminative dictionary designed by learning vector quantization," *IEEE Trans. Geosci. Remote Sens.*, vol. 52, no. 8, pp. 4808–4822, Aug. 2014.
- [30] C. Yu, L.-C. Lee, C.-I. Chang, B. Xue, M. Song, and J. Chen, "Band-specified virtual dimensionality for band selection: An orthogonal subspace projection approach," *IEEE Trans. Geosci. Remote Sens.*, vol. 56, no. 5, pp. 2822–2832, May 2018.
- [31] L. Mou, P. Ghamisi, and X. Xiang Zhu, "Unsupervised spectral-spatial feature learning via deep residual Conv–Deconv network for hyperspectral image classification," *IEEE Trans. Geosci. Remote Sens.*, vol. 56, no. 1, pp. 391–406, Jan. 2018.
- [32] Q. Ling, Y. Guo, Z. Lin, L. Liu, and W. An, "A constrained sparse-representation-based binary hypothesis model for target detection in hyperspectral imagery," *IEEE J. Sel. Topics Appl. Earth Observ. Remote Sens.*, vol. 12, no. 6, pp. 1933–1947, Jun. 2019.
- [33] T. G. Kolda and B. W. Bader, "Tensor decompositions and applications," *SIAM Rev.*, vol. 51, no. 3, pp. 455–500, Aug. 2009.
- [34] J. M. Murphy and M. Maggioni, "Unsupervised clustering and active learning of hyperspectral images with nonlinear diffusion," *IEEE Trans. Geosci. Remote Sens.*, vol. 57, no. 3, pp. 1829–1845, Mar. 2019.
- [35] J. Huang, T.-Z. Huang, L.-J. Deng, and X.-L. Zhao, "Joint-sparse-blocks and low-rank representation for hyperspectral unmixing," *IEEE Trans. Geosci. Remote Sens.*, vol. 57, no. 4, pp. 2419–2438, Apr. 2019.
- [36] N. Kumar and R. Sinha, "Genetic algorithm optimized structured dictionary for discriminative block sparse representation," *IEEE Access*, vol. 8, pp. 19058–19073, 2020.
- [37] K. Tan, S. Zhou, and Q. Du, "Semisupervised discriminant analysis for hyperspectral imagery with block-sparse graph," *IEEE Geosci. Remote Sens. Lett.*, vol. 12, no. 8, pp. 1765–1769, Aug. 2015.
- [38] T. Imbiriba, R. A. Borsoi, and J. C. M. Bermudez, "Low-rank tensor modeling for hyperspectral unmixing accounting for spectral variability," *IEEE Trans. Geosci. Remote Sens.*, vol. 58, no. 3, pp. 1833–1842, Mar. 2020.
- [39] B. Feng and J. Wang, "Hyperspectral image dimension reduction using weight modified tensor-patch-based methods," *IEEE J. Sel. Topics Appl. Earth Observ. Remote Sens.*, vol. 13, pp. 3367–3380, Jun. 2020.
- [40] Y.-J. Deng, H.-C. Li, X. Song, Y.-J. Sun, X.-R. Zhang, and Q. Du, "Patch tensor-based multigraph embedding framework for dimensionality reduction of hyperspectral images," *IEEE Trans. Geosci. Remote Sens.*, vol. 58, no. 3, pp. 1630–1643, Mar. 2020.
- [41] X. Kang, P. Duan, and X. Xiang, "Detection and correction of mislabeled training samples for hyperspectral image classification," *IEEE Trans. Geosci. Remote Sens.*, vol. 56, no. 10, pp. 5673–5686, Oct. 2018.
- [42] J. M. Haut, M. E. Paoletti, J. Plaza, A. Plaza, and J. Li, "Visual attention-driven hyperspectral image classification," *IEEE Trans. Geosci. Remote Sens.*, vol. 57, no. 10, pp. 8065–8080, Oct. 2019.
- [43] W. Zhang, X. Lu, and X. Li, "Similarity constrained convex non-negative matrix factorization for hyperspectral anomaly detection," *IEEE Trans. Geosci. Remote Sens.*, vol. 57, no. 7, pp. 4810–4822, Jul. 2019.
- [44] X. Yang, J. Chen, and Z. He, "Sparse-SpatialCEM for hyperspectral target detection," *IEEE J. Sel. Topics Appl. Earth Observ. Remote Sens.*, vol. 12, no. 7, pp. 2184–2195, Jul. 2019.
- [45] W. Li, Q. Du, and B. Zhang, "Combined sparse and collaborative representation for hyperspectral target detection," *Pattern Recognit.*, vol. 48, no. 12, pp. 3904–3916, Dec. 2015.
- [46] A. W. Bitar, L.-F. Cheong, and J.-P. Ovarlez, "Sparse and low-rank matrix decomposition for automatic target detection in hyperspectral imagery," *IEEE Trans. Geosci. Remote Sens.*, vol. 57, no. 8, pp. 5239–5251, Aug. 2019.
- [47] J. Frontera-Pons, F. Pascal, and J.-P. Ovarlez, "Adaptive nonzero-mean Gaussian detection," *IEEE Trans. Geosci. Remote Sens.*, vol. 55, no. 2, pp. 1117–1124, Feb. 2017.
- [48] Y. Ma, C. Li, X. Mei, C. Liu, and J. Ma, "Robust sparse hyperspectral unmixing with $\ell_{2,1}$ norm," *IEEE Trans. Geosci. Remote Sens.*, vol. 55, no. 3, pp. 1227–1239, Mar. 2017.
- [49] S. Mei, J. Ji, J. Hou, X. Li, and Q. Du, "Learning sensor-specific spatial-spectral features of hyperspectral images via convolutional neural networks," *IEEE Trans. Geosci. Remote Sens.*, vol. 55, no. 8, pp. 4520–4533, Aug. 2017.
- [50] C. McCann, K. S. Repasky, M. Morin, R. L. Lawrence, and S. Powell, "Using landsat surface reflectance data as a reference target for multiswath hyperspectral data collected over mixed agricultural rangeland areas," *IEEE Trans. Geosci. Remote Sens.*, vol. 55, no. 9, pp. 5002–5014, Sep. 2017.
- [51] Y. Niu and B. Wang, "Extracting target spectrum for hyperspectral target detection: An adaptive weighted learning method using a self-completed background dictionary," *IEEE Trans. Geosci. Remote Sens.*, vol. 55, no. 3, pp. 1604–1617, Mar. 2017.
- [52] Z. Dong, M. Wang, Y. Wang, Y. Zhu, and Z. Zhang, "Object detection in high resolution remote sensing imagery based on convolutional neural networks with suitable object scale features," *IEEE Trans. Geosci. Remote Sens.*, vol. 58, no. 3, pp. 2104–2114, Mar. 2020.
- [53] S. Aksoy, H. G. Akcay, and T. Wassenaar, "Automatic mapping of linear woody vegetation features in agricultural landscapes using very high resolution imagery," *IEEE Trans. Geosci. Remote Sens.*, vol. 48, no. 1, pp. 511–522, Jan. 2010.
- [54] M. Wang, Z. Dong, Y. Cheng, and D. Li, "Optimal segmentation of high-resolution remote sensing image by combining superpixels with the minimum spanning tree," *IEEE Trans. Geosci. Remote Sens.*, vol. 56, no. 1, pp. 228–238, Jan. 2018.
- [55] D. Snyder *et al.*, "Development of a Web-based application to evaluate target finding algorithms," in *Proc. IEEE Int. Geosci. Remote Sens. Symp.*, Boston, MA, USA, Jul. 2008, pp. 915–918.
- [56] J. Kerekes and D. Snyder, *Target Detection Test*. [Online]. Available: <http://dirsapps.cis.rut.edu/blindtest/>
- [57] D. Zhu, B. Du, and L. Zhang, "Target dictionary construction-based sparse representation hyperspectral target detection methods," *IEEE J. Sel. Topics Appl. Earth Observ. Remote Sens.*, vol. 7, no. 4, pp. 1254–1264, Apr. 2019.
- [58] T. Guo, F. Luo, L. Zhang, X. Tan, J. Liu, and X. Zhou, "Target detection in hyperspectral imagery via sparse and dense hybrid representation," *IEEE Geosci. Remote Sens. Lett.*, vol. 17, no. 4, pp. 716–720, Apr. 2020.
- [59] F. Luo, B. Du, L. Zhang, L. Zhang, and D. Tao, "Feature learning using spatial-spectral hypergraph discriminant analysis for hyperspectral image," *IEEE Trans. Cybern.*, vol. 49, no. 7, pp. 2406–2419, Jul. 2019.



Chunhui Zhao received the B.S. and M.S. degrees from Harbin Engineering University, Harbin, China, in 1986 and 1989, respectively, and the Ph.D. degree from the Department of Automatic Measure and Control, Harbin Institute of Technology, Harbin, in 1998.

He was a Post-Doctoral Research Fellow with the College of Underwater Acoustical Engineering, Harbin Engineering University, where he is working with the College of Information and Communication Engineering, as a Professor and Doctoral Supervisor.

His research interests include digital signal and image processing, mathematical morphology and hyperspectral remote sensing image processing.

Prof. Zhao is a senior member of Chinese Electronics Academy.



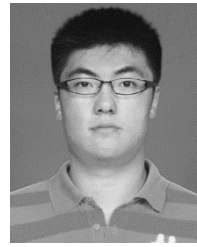
Shou Feng received the Ph.D. degree from the Harbin Institute of Technology, Harbin, China, in 2019.

He is an Assistant Professor with Harbin Engineering University, Harbin. His main research interests include remote sensing image processing, data mining, machine learning, and so on.



Mingxing Wang is pursuing the Ph.D. degree with Harbin Engineering University, Harbin, China.

His main research areas are hyperspectral image processing and so on.



Nan Su received the Ph.D. degree from the Harbin Institute of Technology, Harbin, China, in 2017.

He is an Associate Professor with Harbin Engineering University, Harbin. His main research areas are remote sensing image processing, data mining, and so on.